Suspension dynamics of sand-silt mixtures
experimental insights and modelling implications

Qiao, Zhongxing; Chen, Yongping; Yao, Peng; Su, Min; Stive, Marcel; Ren, Lei; Wang, Zhengbing

DOI
10.1016/j.jhydrol.2025.133836

Publication date
2025

Document Version
Final published version

Published in
Journal of Hydrology

Journal of Hydrology 661 (2025) 133836

Contents lists available at ScienceDirect

Journal of Hydrology

journal homepage: www.elsevier.com/locate/jhydrol

Research papers

Suspension dynamics of sand-silt mixtures: experimental insights and modelling implications

Zhongxing Qiao [a,c], Yongping Chen [a,c], Peng Yao [a,b,*], Min Su [a,c], Marcel Stive [d], Lei Ren [e], Zhengbing Wang [d,f]

[a] National Key Laboratory of Water Disaster Prevention, Hohai University, Nanjing 210098, China
[b] Key Laboratory of Ocean Space Resource Management Technology, MNR, China
[c] College of Harbour, Coastal and Offshore Engineering, Hohai University, 1 Xikang Road, Nanjing 210098, China
[d] Faculty of Civil Engineering and Geosciences, Section of Hydraulic Engineering, Delft University of Technology, P.O. Box 5048, 2600 GA Delft, the Netherlands
[e] School of Ocean Engineering and Technology, Sun Yat-sen University, China
[f] Deltares, P.O. Box 177, 2600 MH Delft, the Netherlands

ARTICLE INFO

This manuscript was handled by marco borga, Editor-in-Chief, with the assistance of Edward Park, Associate Editor

Keywords:
Silt-dominated sediment
Silt content
Equilibrium concentration
Suspension process
Annular flume experiment

ABSTRACT

Tidal flats are typically rich in fine-grained sediments, with tidal currents serving as the dominant hydrodynamic force. Sediment transport, mainly in the form of suspended load, is especially active in the mid- to low-tidal zones, where silt-rich sediments prevail. In these zones, variations in silt content significantly influence sediment suspension dynamics. To investigate the effect of silt content on the suspension behaviours of sand-silt mixtures under unidirectional flow, a series of experiments has been conducted in an annular flume. Sediment samples collected from silt-enriched tidal flats were remixed into seven types of sediment beds with the silt content ranging from 19 % to 79 %. Results indicate that under steady current conditions, the suspended sediment concentration (SSC) in sand-silt mixtures increased toward equilibrium. Sediment beds with 36 %–60 % silt content exhibited two-stage erosion behaviour, each marked by distinct characteristics. At low to moderate shear stress (0.18–0.74 Pa), smoother bed surfaces and hiding-exposure effects led to higher near-bed velocities and lower equilibrium SSCs. At higher shear stress levels (1.00–1.23 Pa), this behaviour shifted, with prolonged suspension development becoming the key feature. Based on the experimental findings, we further re-calibrated the equations predicting equilibrium SSC, which can be well described by a modified excess shear stress to the power of two. Subsequently, we investigated the boundary conditions that govern sediment suspension to model the observed suspension process. Building on the boundary condition prescribing a constant upward sediment flux, an asymptotic upward flux condition, which represents the delayed erosion response due to the resistance of silty bed structure, has been introduced and demonstrated as the most feasible. Furthermore, the development of SSC towards equilibrium was investigated. This process is well characterised by a time scale, which becomes notably larger for sediment beds with 36 %–60 % silt content at high velocity levels, reflecting their delayed response in suspension. These findings elucidate key mechanisms governing silt-dominated sediment erosion, enhancing predictive capabilities in modelling mixed sediment transport.

1. Introduction

Tidal flat sediments are typically fine-grained and exhibit complex and heterogeneous grain-size distributions, consisting mainly of clay, silt, and fine sand. The composition of surface sediments varies across tidal flat zones: clayey silt with higher cohesion is commonly found in the upper intertidal areas, while sand–silt mixtures with lower cohesion dominate the middle to lower intertidal zones, where sediment transport is especially active (Gao, 2019; Wang and Zhu, 1990). Variation in sediment composition leads to distinct transport behaviours and dynamic responses to hydrodynamic forces. As a regular and persistent hydrodynamic force in tidal flat regions, tidal currents serve as a major driver for sediment transport (Dinehart and Burau, 2005; Zhang et al., 2024; Zhou et al., 2021; Zhu et al., 2024). Sediment transport in these environments is primarily in the form of suspended load (Xing et al., 2022), which plays a crucial role in coastal eco- and morpho-dynamics.

* Corresponding author at: National Key Laboratory of Water Disaster Prevention, Hohai University, Nanjing 210098, China.
E-mail address: p.yao@hhu.edu.cn (P. Yao).

https://doi.org/10.1016/j.jhydrol.2025.133836
Received 8 February 2025; Received in revised form 16 June 2025; Accepted 3 July 2025
Available online 5 July 2025

Ecologically, suspended sediment can act as a transport medium for pollutants, posing risks to aquatic ecosystems (Chen et al., 2021a). Morphologically, the transport of suspended sediment leads to erosion or deposition, driving the morphological evolution of tidal flats. Therefore, this study focuses on suspension dynamics of sand-silt mixtures under current conditions. The findings can offer deeper insights into sediment transport mechanisms and their associated ecological–morphological responses in coastal environments.

Historically, numerous laboratory experiments were conducted to understand erosion processes by currents. For non-cohesive sand, erosion begins when the bed shear stress exceeds the erosion threshold, and reaches a steady state when the suspended sediment concentration (SSC) attains the carrying capacity of the flow. Under normal current conditions, particles are picked up individually (van Rijn, 1984; Cao, 1997); while during calamity-type flow conditions, they are entrained in layers (Mastbergen and Berg, 2003; van Rhee, 2010). For non-cohesive sand, the near-bed zone is often considered to respond rapidly to hydrodynamic conditions. Accordingly, a common modelling approach is to prescribe a constant upward sediment flux at the bed (Celik and Rodi, 1988; Reed et al., 1999; Hu et al., 2020; Hu et al., 2025). This prescribed flux is directly related to the equilibrium near-bed SSC, i.e., the reference concentration, which therefore plays a crucial role in modelling non-cohesive sediment transport.

The reference concentration in noncohesive sediment transport models is typically formulated as a function of a near-bed hydrodynamic parameter. Since the concept of critical shear stress (τ_{cr}) being recognised by Shields (1936), the excess shear stress, which is the dynamic component of bed shear stress available to entrain sediment beyond a critical threshold ($\tau_b - \tau_{cr}$), has been integrated into bed load transport formulas such as the MPM formula (Meyer-Peter and Muller, 1948). Parallelly, for the reference concentration for suspended load, many formulations implicitly or explicitly relied on the concept of excess shear stress (Einstein, 1950; Engelund and Fredsøe, 1976; Smith and McLean, 1977; van Rijn, 1984; Wright and Parker, 2004).Meanwhile, alternative approaches employed dimensionless suspension parameters such as the ratio of friction velocity and settling velocity (u_*/w_s) to describe the capacity of turbulence to maintain sediment in suspension (Celik and Rodi, 1988; García and Parker, 1991), offering a more turbulence-centric view of reference concentration. Although these formulations did not involve critical shear stress directly, but still assumed a threshold-like behaviour through settling velocity. More recently, through flume experiments, Diplas et al. (2008) recognised the importance of impulse in the initiation of motion for sediment particles of millimetre scale. However, whether impulse can be applied to describe the suspension of fine sediments remains unclear. Recognizing the heterogeneous nature of natural sediment beds, researchers have long incorporated effects caused by mixed sediments, such as the hiding and exposure effect. Egiazaroff (1965) was among the first to introduce this concept into theoretical functions for suspended sediment concentration (SSC), and similar interaction-based effects were incorporated into successive formulations (García and Parker, 1991; McLean, 1992; Wright and Parker, 2004; de Leeuw et al., 2020). These models typically consider the relative mobility of different sediment fractions, with interactions described through functions of grain-size ratios or other indicators of size distribution. Beyond interaction effects, other models have emphasized the influence of specific grain-size fractions on suspension behaviour. Wilcock (1998) developed a two-fraction model that quantifies how the transport of gravel is affected by the presence of sand. Later on, van Rijn (2007b) explicitly introduced both clay and silt fractions into the reference concentration formulation, which considers the suppressing and promoting effect of clay and silt on suspension respectively, and has since been adapted for sand–silt mixtures under wave conditions (Yao et al., 2015).

For cohesive clayey beds, which are different from the above-mentioned non-cohesive beds, the erosion process can be categorised into three modes: floc erosion, surface erosion and mass erosion. Floc erosion occurs probabilistically when local bed shear stress exceeds the erosion threshold, even if the mean bed shear stress τ_b is lower than the critical bed shear stress τ_{cr} (Parchure and Mehta, 1985; Winterwerp et al., 2012). Surface erosion occurs when τ_b significantly exceeds τ_{cr} in a drained bed scenario, mobilizing sediment layers simultaneously. In contrast, under undrained conditions, pore pressure dominates the process of erosion, potentially causing sediment lumps to be abruptly torn from the bed when τ_b surpasses the undrained bed strength. Among the three modes, surface erosion is the most common and significantly contributes to cohesive sediment transport (Chen et al., 2022). Based on the variance of τ_{cr} with depth, surface erosion can be further divided into two types. For sediment where τ_{cr} increases with depth (Type I), erosion ceases at a certain depth where τ_{cr} exceeds bed shear stress τ_b; for uniform sediment bed (Type II), τ_{cr} remains unchanged with depth, and once τ_b surpasses τ_{cr}, erosion continues without interruption (Mehta & Partheniades, 1982; Sanford and Maa, 2001; Stone et al., 2008). For cohesive sediments, the equilibrium concentration is often termed as saturation concentration (Winterwerp, 2001). An existence example of saturation concentration for steady flow condition is the Yellow River. However, this saturation concentration is rarely served as bed boundary conditions in simulating suspension process of cohesive bed. Meanwhile, the erosion rate, with excess shear stress as the decisive hydrodynamic factor, becomes a key factor regarding modelling cohesive sediment transport (Berlamont et al., 1993; Parchure and Mehta, 1985; van Prooijen and Winterwerp, 2010; Walder, 2016).

Due to the diversity in tidal flat sediment composition, which includes sand, silt, and clay (silt and clay are collectively referred to as mud), many studies have focused on dynamic properties of sand-mud mixtures. The influence of fine composition on reducing erosion was early highlighted by Murray (1976). Mitchener and Torfs (1996) observed a transition of erosion mode when mud content ranged from 3 % to 15 %, while Panagiotopoulos et al. (1997) observed an erosion regime alteration around 30 % mud content, and Houwing (2000) spotted a transition of erosion behaviour as the mud content ranged from 20 % to 30 %. Banasiak and Verhoeven (2008) suggested that even a small proportion (3–10 %) of cohesive component can remarkably reduce the transport rates in comparison to a pure sand. Recently, Perkey et al. (2020) conducted a series of erosion experiments on three types of mixtures with different mineral compositions, finding that erosion rates decreased by 1 to 2 orders of magnitude as mud content approached 5 %, reaching a minimum around 30–40 % mud content. Despite the variations in reported critical mud content thresholds for erosion transitions, cohesive properties are primarily associated with fine silt and clay within the mud. Van Ledden et al. (2004) proposed that clay content, rather than overall mud content, is a more reliable indicator of erosion behaviour, with most studies identifying a critical clay content range between 5 % and 10 %. In addition to cohesive composition, bulk density is another crucial factor influencing the erosion rate, particularly in mixtures with high mud content (Gailani et al., 2001; Roberts et al., 1998; Torfs, 1995; van Rijn, 2020), profoundly influencing erosion rate predictions (Aberle et al., 2004; Chen et al., 2018; Perera et al., 2020).

Extended research has been conducted on the erosion and suspension of sand, clay, and sand-clay mixtures. However, silt content (8–62.5 μm; van Rijn, 2007a) is abundantly found in tidal flat regions like the Yellow River Delta and central Jiangsu Coast—with silt contents ranging from 48-85 % (Jia et al., 2020) and 10–80 % (Kuai et al., 2021), respectively—has received comparatively less attention. As a transitional sediment fraction between cohesive clay and non-cohesive sand, silt is often described as pseudo-cohesive. Although primarily composed of cohesionless minerals like feldspar and quartz, silt exhibits cohesive-like properties, such as critical shear stress being dependent on bulk density, as observed in previous erosion tests (Roberts et al., 1998; Yao et al., 2022a). Despite these cohesive-like behaviours, flocculation has not been observed in settling experiments (te Slaa et al., 2013, 2015). Previous studies on silt dynamics have mainly focused on its erosion

threshold and behaviours under wave conditions. Regarding its erosion threshold, several studies (Dong, 2007; Jacobs et al., 2011; Bartzke et al., 2013) found that adding silt into sand can increase the critical shear stress of bimodal sand-silt mixtures, and Yao et al. (2018) demonstrated that increasing of silt fraction in unimodal sand-silt mixtures similarly raises the threshold of motion. Later, Yao et al. (2022a) modified the Shields curve to estimate the critical shear stress of silt-dominated sediments. As for silt's behaviours under wave conditions, Yao et al. (2015) predicted the equilibrium reference concentration of sand-silt mixtures, followed by Zuo et al. (2019, 2021), modelling the vertical profile of SSC and depth-averaged SSC. However, despite these advances, the suspension process of silt-dominated sediments under current remains poorly understood. Since tidal flats are essentially influenced by tidal currents, it is critical to investigate how silt-dominated sediment behaves under current, particularly regarding the development of SSC over time and the equilibrium SSC. Existing equilibrium SSC models were developed based on non-cohesive sands and may not adequately capture the suspension behaviour of silt.

To address this gap, a series of annular flume experiments was conducted with seven mixed beds of different sand-silt compositions, focusing on the following scientific questions: How does silt content influence the suspension process? Can the SSC of silt-dominated mixtures reach an equilibrium state under steady current? If equilibrium exists, how can the equilibrium SSC be estimated, and how can the process of SSC development toward equilibrium be described? Specifically, this paper is structured as follows: Section 1 introduces the study. Section 2 details the experimental procedure and the relevant sediment transport modelling background. Section 3 analyses the experimental results. Section 4 discusses the estimation of equilibrium SSC and the numerical prediction of the suspension process. Finally, Section 5 presents the conclusions.

2. Materials and methods

2.1. Sediment samples

The sediment mixtures used in the experiments were collected from a silt-dominated tidal flat located in the central Jiangsu coast, China. After being washed, dried, and sorted using sieves and a centrifuge, the sediment samples were re-mixed into seven groups, with silt content ranging from 19 % to 79 %. According to van Rijn (2007a) and Yao et al. (2015), a significant cohesive fraction remains in very fine silt with grain sizes between 4 and 8 μm. Therefore, in this study, particles ranging from 8 to 62 μm are classified as silt, while those smaller than 8 μm are defined as clay. As suggested by van Ledden et al. (2004), sediment mixtures demonstrate noticeable cohesive behaviour when clay content exceeds 5 %~10 %. To minimise the cohesive effects in the mixtures used in this study, clay content was kept below 5 % by limiting particles smaller than 8 μm. The grain-size distribution curves of sediment mixtures measured by laser particle analyser Malvern Mastersizer 3000 are shown in Fig. 1. The properties of sediment mixtures are listed in Table 1, with the critical shear stress data derived from the experimental results of Yao et al. (2022a).

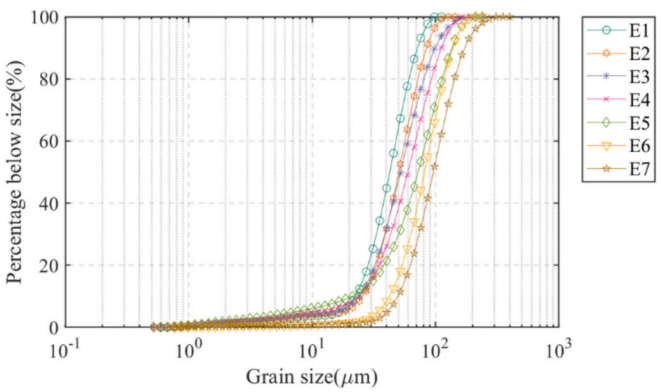

Fig. 1. Grain size distributions of sand-silt mixtures.

2.2. Annular flume experiments

The experiments were conducted in the annular flume at Hohai University, China. Annular flumes are an ideal equipment for studying fine-grained sediment dynamics, as the closed design prevents sediment loss and allows for the generation of a uniform unidirectional flow that mimics an infinitely long channel, providing stable conditions for analysis. The flume consists of three main components: an upper ring, a flume base, and a power system (Fig. 2). The outer and inner diameters of the flume are respectively 2.8 m and 2.4 m, with a channel width of 0.2 m between the walls. During the experiments, the lower surface of lid was adjusted to cling to the surface of water to set water in motion by rotation of the lid. To offset the influence of secondary flows caused by the shape of the flume, the lid and flume base rotated in opposite directions simultaneously by a pre-calibrated rotation rate ratio (Yao et al., 2018). In total 7 experiments were conducted, each corresponding to different sand-silt compositions of the sediment. In each experimental group, 10 velocity levels (0.04–0.47 m/s) were discretely applied. This velocity range corresponds to the near-bed velocities observed on the typical tidal flats of the Jiangsu coast (Zhang et al., 2016). Each experiment was performed 3 times to assess repeatability.

The experiments were conducted in fresh water conditions. It is noted that in coastal waters, the salinity may exert the flocculation effects of fine-grained sediments. Based on settling experiment of silt-sized sediments, no flocculation can be observed for silt grains larger than 40 μm in saline water environment (with salinity of 2–35 ‰), and weak flocculation were observed for grains ranging from 8 to 40 μm (Yao et al., 2022b). Since the sediment particles with size smaller than 8 μm was kept below 5 % of each sediment bed, the effect of salinity on the sediment flocculation can be considered negligible.

The near-bed current velocity was measured by an Acoustic Doppler Velocimetry (Nortek, Vectrino Profiler II), capable of obtaining 35 mm-thick velocity profiles at a sampling frequency of 25 Hz. Turbidity signals of SSCs were recorded by six Infrared Backscatter Sensors (IBSs) installed at various elevations along the inner wall of the flume. These sensors were positioned at heights of 5.45, 7.25, 9.70, 11.70, 14.10, and 15.55 cm above the flume bottom. Each sensor was paired with a sampling hole, with two additional sampling holes located at 3.4 cm and 9.7 cm above the bottom. Thus, water samples were collected through the eight tubes when the IBS signals reached a steady state. These samples were processed by both pycnometer and filtration method independently to determine SSCs, which were further utilised to calibrate IBS outputs and obtain SSC time series. The grain sizes of the collected samples were then measured by the laser particle analyser (see Supplementary Material Table 1).

The adopted procedure of the experiments has been as follows:

(1) Stir the sediment sample and water into slurry, spread the slurry on the bottom of the flume up to 2.5 cm thick to form the sediment bed, and scrape the surface of the bed to ensure its flatness.

Table 1
Properties of sand-silt mixtures.

Name	E1	E2	E3	E4	E5	E6	E7
P_{clay} (<8 μm)/%	3	3	4	4	5	1	1
P_{silt} (8–62.5 μm)/%	79	66	60	49	36	29	19
P_{sand} (>62.5 μm)/%	18	31	36	47	59	70	80
D_{50} /μm	42.6	50.4	52.0	59.7	72.2	81.6	96.9
D_{90}/D_{10}	3.2	3.3	4.1	4.7	6.5	3.3	3.5
τ_{cr} /Pa	0.19	0.21	0.21	0.19	0.19	0.12	0.10

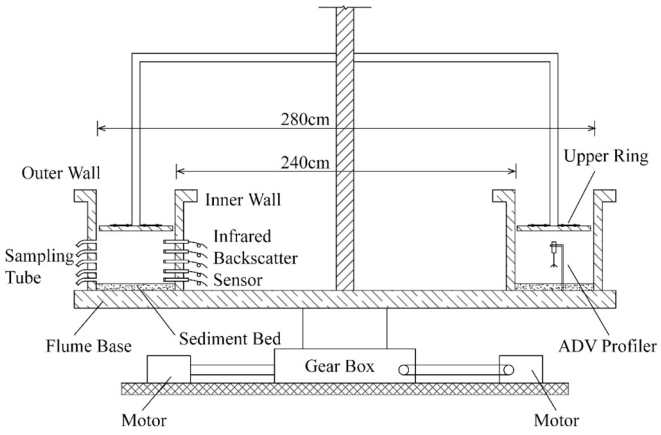

Fig. 2. Schematic of the annular flume and experimental setup.

(2) Fill the flume with fresh water to a depth of 30 cm, and allow the sediment to consolidate for 2 h, which is sufficient for the bulk density to stabilize (based on the compaction experiment of Yao et al., 2022a).
(3) Switch on all data acquisition devices (i.e., ADV and IBS), turn on the power of annular flume, and adjust the rotation rate of upper ring and flume base to predetermined speed.
(4) Once the IBS signals stabilize, collect water samples from sampling holes at different elevations. After sampling, adjust the rotation rate to the next level.
(5) Upon completion of the experiment, clean the flume and proceed with either the repeatability test or the next experiment using a new sediment sample, starting from step (1).

Owing to the different sediment bed types, the time-averaged near-bed velocities vary over different sediment beds, even at the same flow velocity level. To represent the hydrodynamic conditions in a unified manner, the near-bed velocity and shear stress under clean water conditions are used, as listed in Table 2. The bed forms of different beds, which evolved in case of large velocity levels, are detailed in Table 3.

2.3. Data processing

Time-averaged near-bed velocity and bed shear stress can be determined from 3D velocity data measured by ADV. The velocity data were first filtered to remove poor-quality measurements (beam correlations < 70 % and SNR < 12) and then despiked using the phase-space threshold method (Goring and Nikora, 2002; Yao et al., 2022a). According to Staudt et al. (2019), a thin turbulent boundary layer exists in an annular flume, and the velocity at 1 cm above the bed falls within this layer for calculating near-bed velocity and bed shear stress. Therefore, in this study, velocity data at 1 cm above the bed were used. Moving average was adopted as the smoothing method to separate mean velocity $\overline{u}$ and velocity fluctuations u' (see Supplementary Material Fig. 1). Thompson et al. (2004) and Pope et al. (2006) recommended using Turbulence Kinetic Energy (TKE) approach to calculate bed shear stress in annular flume conditions. Through this approach, the velocity at a fixed elevation within the bottom boundary layer is taken for calculation to avoid the influence of bed level change in sediment experiment. The TKE is expressed as:

Table 3
Observed bed forms at different velocity levels.

Bedform sediment	Velocity level					
	1–5	6	7	8	9	10
E1	Plane	Micro ripples	Ripples growing	Maximum size	Ripples eroded	Plane
E2	Plane	Micro ripples	Ripples growing	Maximum size	Ripples eroded	Further eroded
E3	Plane	Plane	Micro ripples	Ripples growing	Maximum size	Ripples eroded
E4	Plane	Plane	Micro ripples	Ripples growing	Maximum size	Ripples eroded
E5	Plane	Plane	Micro ripples	Ripples growing	Maximum size	Plane
E6	Plane	Micro ripples	Ripples growing	Ripples growing	Maximum size	Ripples eroded
E7	Plane	Micro ripples	Ripples growing	Ripples growing	Maximum size	Ripples eroded

$$TKE = \rho\left(\overline{u_x'^2} + \overline{u_y'^2} + \overline{u_z'^2}\right)/2 \quad (1)$$

$$\tau = C_1 \cdot TKE \quad (2)$$

where u_x', u_y', u_z' denote the steam-wise, cross-channel and vertical components of velocity fluctuations, ρ is the water density and τ is the bed shear stress. The bed shear stress is related to TKE through constant$C_1 = 0.19$ as suggested by Pope et al. (2006).

Depth-averaged suspended sediment concentration (SSC) time series can be acquired through IBS data (see Supplementary Material Fig. 2). The fluctuations of signal were first filtered out by moving average method, and the signals at (quasi-) steady state can be recognized at the end of the curve. The steady IBS signals indicated the establishment of an equilibrium state for sediment concentration. Subsequently, water samples collected during steady state at different elevations above the bed were filtered, dried and weighed to acquire SSCs, which were then used to calibrated IBS signals. By correlating the steady IBS signal with equilibrium SSC, the IBS signals were converted to SSC time series. The depth-averaged SSC time series was obtained by first integrating the SSC time series across all elevations, then calculating the average value over the depth.

3. Results

3.1. Variations of near-bed velocity over different sediment beds

In the annular flume, the velocity in streamwise direction is the major component while the velocity magnitudes in the other two directions were relatively small. Thus, only the streamwise component of flow velocity is considered. Note that at velocity level 10, the high SSC leads to the larger noise in water, leading to the poor quality of ADV data (SNR < 12), thereby excluded. The absence of flow velocity data at this level does not affect the analysis of the experimental results, since the velocity magnitude of each level was mainly used as a representation of the hydrodynamic condition. Fig. 3 shows the near-bed velocities at velocity levels 1–9 over different sediment beds (represented by different silt contents), which were taken from 1 cm above the bed.

At velocity levels 1–3, near-bed velocity increases slightly as the silt content in the sediment bed rises. This occurs because, under slow flow conditions, the sediment beds remain flat, and bed roughness is

Table 2
Near-bed flow velocity and the corresponding shear stress in clean water.

Velocity level	1	2	3	4	5	6	7	8	9	10
Velocity (m/s)	0.04	0.07	0.08	0.14	0.17	0.20	0.26	0.35	0.39	0.47
Shear stress (Pa)	0.02	0.05	0.08	0.18	0.26	0.34	0.51	0.70	1.00	1.23

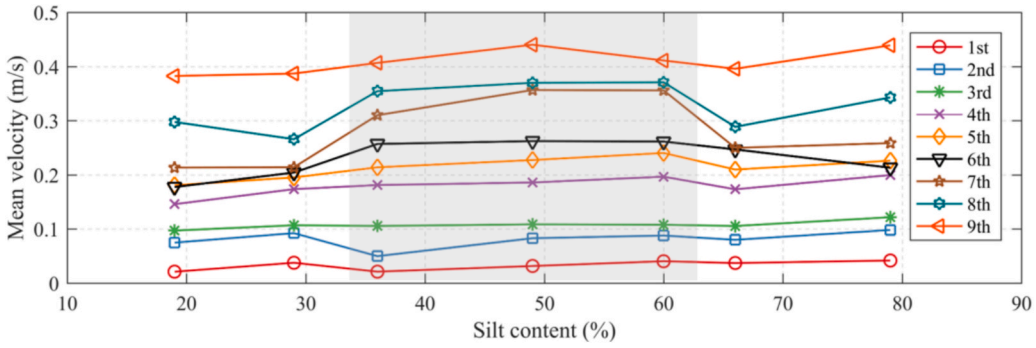

Fig. 3. Mean velocity at 1 cm above bed surface during experiment with sediments with various silt contents at velocity levels 1–9.

primarily governed by skin friction, which is closely related to grain size. Smaller grain sizes result in reduced bed friction, allowing for higher velocities near the bed. At velocity levels 4–8, the near-bed velocities over sediments with silt content ranging from 36 % to 60 % (E3-E5) are relatively higher than the others, with this trend becoming more pronounced as velocity increases (Shadowed area in Fig. 3). At this stage, grain size is no longer the primary factor affecting bed roughness, as the sediment bed is mobilised. Instead, the nonuniformity of sediment gradation plays a significant role. The larger nonuniformity in sediments E3-E5 leads to smoother bed surfaces, resulting in higher current velocities over these sediments. At velocity level 9, as the flow shear stress largely overwhelms the strength of sediment bed, the near-bed current velocities over different sediment exhibit similar magnitudes.

3.2. Variations of SSCs over different sediment beds

Fig. 4 illustrates the development of SSC at velocity levels 7 to 10, when noticeable suspension occurred over different sediment beds. Generally, SSC rises with a diminishing growth rate until it eventually reaches a steady state with minimal fluctuations (viz. equilibrium SSC). Herein, we term this development period of SSC as suspension process. The suspension processes can be classified into two types. The first type, observed in sediments with p_{silt} of 36 %-60 % (E3-E5), exhibits a slower initial growth rate and a longer duration to reach equilibrium. The second type, observed in sediments E1, E2, E6, and E7, shows higher initial erosion rates but attains equilibrium quickly. This distinction becomes more pronounced with increasing current velocity. For example, at velocity level 10, SSC of sediment beds with 36 %-60 % p_{silt} takes over 3000 s to reach a steady state, while the SSC of sediment bed

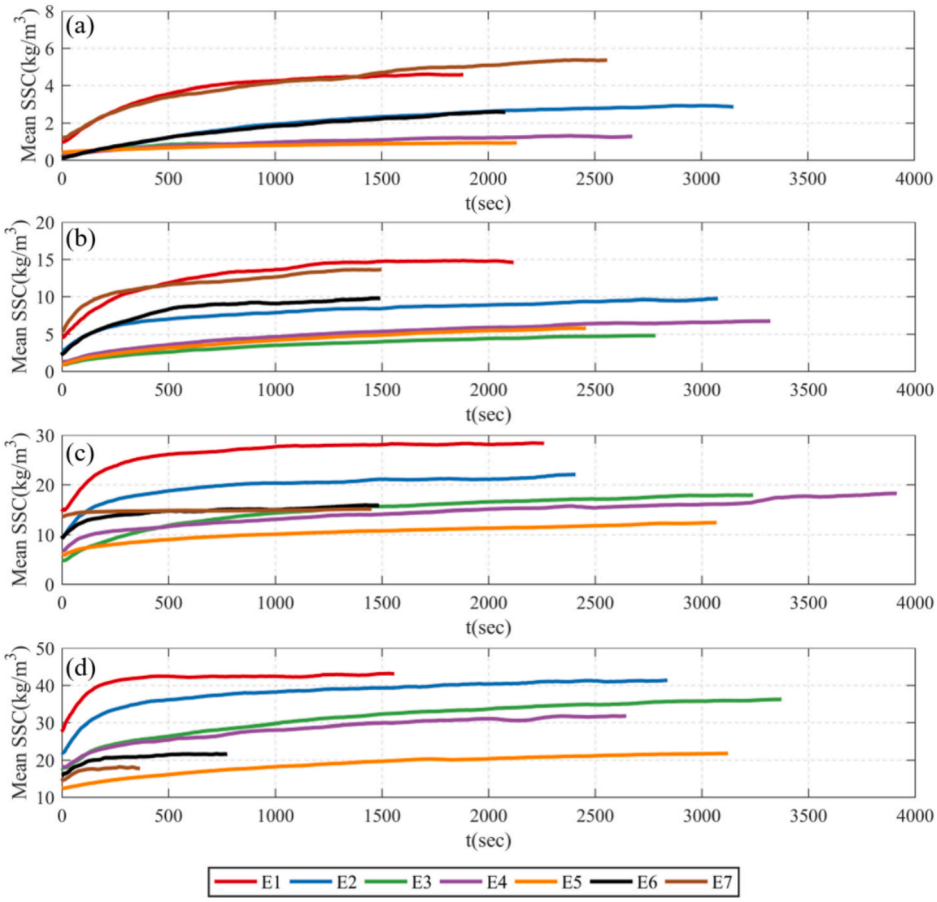

Fig. 4. Development of depth-averaged SSCs at velocity levels 7–10 (a to d) over different sediment beds.

E6 (29 % p_{silt}) takes less than 100 s. The suspension processes of silt-dominated sediment exhibit transitional behaviour between non-cohesive and cohesive sediment. While SSC over silt-dominated sediments can eventually achieve an equilibrium state similar to non-cohesive sand, it takes longer to reach this equilibrium, with SSC showing relatively high growth during the initial suspension stage, resembling cohesive sediment behaviour.

Fig. 5a presents depth-averaged SSCs at steady state (i.e., equilibrium SSC, c_e) over different sediment beds. At velocity levels 7 and 8, with the increase of silt content, c_e initially decreases (p_{silt} 19 %-36 %), then levels off (p_{silt} 36 %-60 %), and finally rises (p_{silt} 60 %-79 %). Notably, sediments with p_{silt} ranging from 36 % to 60 % exhibit similar and comparatively lower c_e than the others. As velocity level moves up, this distinctive pattern in the c_e values for sediments E3-E5 diminishes, and a linear relationship between c_e and p_{silt} emerges, becoming particularly distinguished at velocity level 10. To reveal the sediment response to changing flow conditions, the increment of SSC is analysed. Fig. 5b depicts the equilibrium SSC increments relative to the former velocity level (Δc_e) at velocity levels 7–10. At velocity levels 7–8, the equilibrium SSC increment of sediments with p_{silt} of 36 %-60 % are close and relatively smaller than the rest, which resembles the distribution of c_e (i.e. Fig. 5a). At velocity levels 9–10, the SSC increment almost linearly increases with the rise of p_{silt}. It should be noted that shortage of sediment supply causes some unusual data variations. At velocity level 10, a significant drop in Δc_e is observed for E1. Additionally, the SSC for sediment E7 shows almost no increase at velocity levels 9 and 10. Although the SSCs appear steady in these cases, they do not reflect the actual entrainment capacity and therefore cannot be considered as equilibrium SSCs.

Fig. 6 illustrates the equilibrium profiles of SSCs at velocity levels 7–10, with the experimental data points shown as the scattered dots. The diffusion coefficient exhibits a linear distribution within the elevation range where sediment samples were collected, which is consistent with the findings of Booij and Tukker (1996) regarding turbulent eddy viscosity. Therefore, the SSC profiles are empirically fitted by a series of power functions with the form of $c = c_a \bullet z^m$, in which c_a is the reference concentration at the reference level $z_a = 1$ cm, and m represents the vertical non-uniformity of SSC. The fitted SSC profiles are shown as solid curves in Fig. 6, and the fitted results of c_a and m are shown in Table 4. With the rise of velocity level, the depth-averaged SSC increases and the vertical distribution of SSC appears to be more uniform (i.e., absolute value of m decreases). However, c_a does not always follow this trend, e.g., from velocity level 9 to 10, although the amount of suspension rises, the intensified turbulence enhances vertical mixing, making the changes in c_a of sediment E6 less significant, failing to reflect the overall rising trend in SSC.

4. Discussion

4.1. Effects of silt content on erosion behaviour

As suggested by the results, silt content in sediment bed has a significant influence on current velocity, SSC, and SSC development process, particularly for sediment beds with p_{silt} of 36–60 % (i.e., sediment beds E3-E5). These sediment beds exhibit similar characteristics, including higher near-bed velocity (velocity levels 4–8), lower equilibrium SSC (velocity levels 7–8), and prolonged SSC development process (velocity levels 8–10). E3-E5 exhibit greater grain size nonuniformity (see Table 1, D_{90}/D_{10} of E3-E5), likely contributing to their unique behaviour. Thereby, the following will discuss the reasons for their shared characteristics from the aspect of the interaction of the coarse and fine particles.

At velocity levels 4 to 6, the bed shear stress (0.18–0.34 Pa) has just exceeded the critical bed shear stress, significant suspension did not occur. The current velocities for E3-E5 are larger, which implies that the bed friction is smaller for E3-E5. Bed roughness can be quantified by drag coefficient C_D, which is calculated by $C_D = \tau_b/\rho\overline{u}^2$ (Chen et al., 2021b), where $\overline{u}$ is the mean velocity at 1 cm above bed, τ_b is the bed shear stress. Fig. 7 shows the C_D of different sediment beds before the occurrence of significant suspension. With the controlled data quality criteria used in our study (see Data Processing), and according to previous analyses and error propagation theory (Blanckaert and Lemmin,

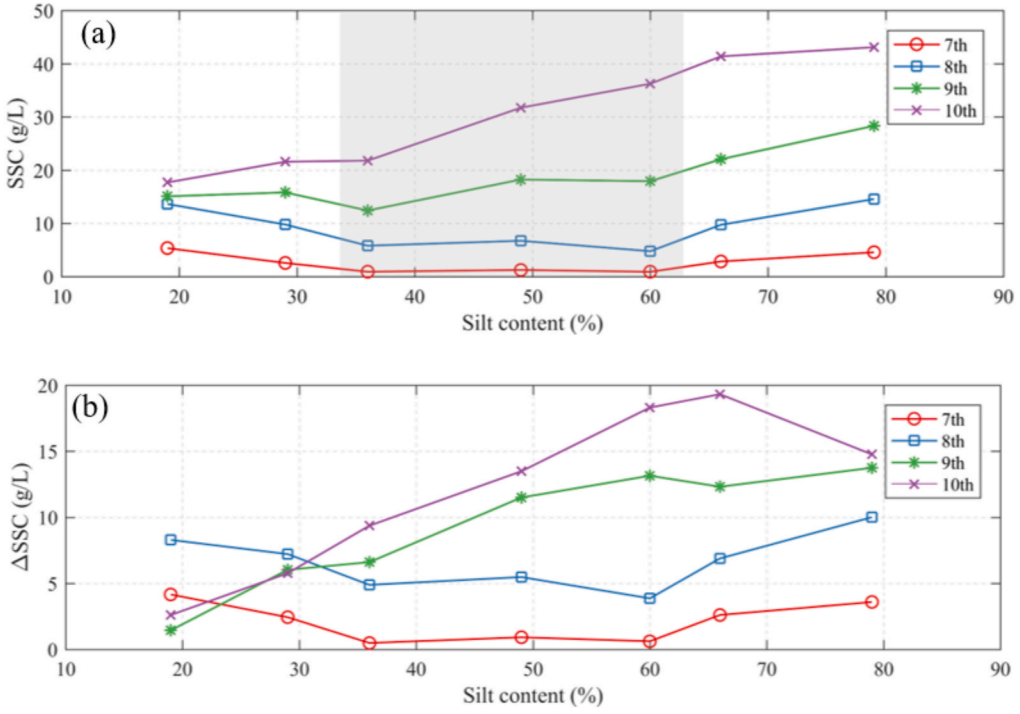

Fig. 5. (a) Depth-averaged SSC at steady state of velocity levels 7–10 over different sediment beds; (b) Equilibrium SSC increments at velocity levels 7–10 over different sediment beds.

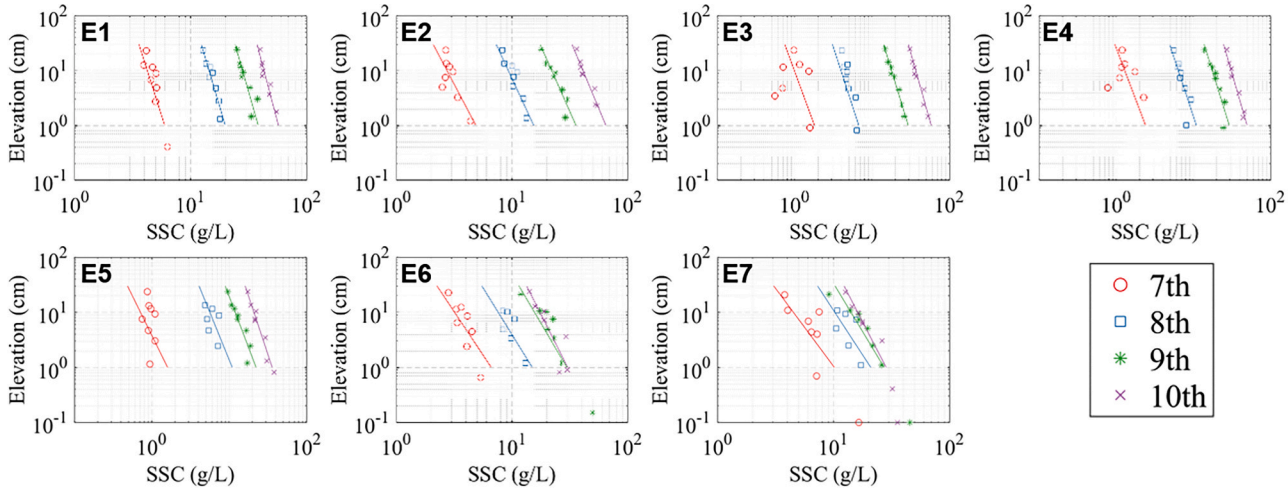

Fig. 6. Vertical distribution of SSCs (scattered dots) and fitting results (solid lines) at velocity levels 7–10 from all experiments in log–log scale.

Table 4
Fitting results of SSC profiles with $c = c_a \bullet z^m$. c_a is the reference concentration at 1 cm above bed, and m represents the nonuniformity of SSC vertical distribution.

m	7th	8th	9th	10th	c_a(g/L)	7th	8th	9th	10th
E1	−0.15	−0.14	−0.14	−0.13	E1	6.00	20.00	38.50	57.50
E2	−0.25	−0.22	−0.21	−0.20	E2	4.88	15.50	36.00	65.26
E3	−0.26	−0.23	−0.22	−0.20	E3	1.80	6.74	29.41	58.35
E4	−0.27	−0.24	−0.22	−0.21	E4	2.40	11.00	29.38	50.00
E5	−0.35	−0.29	−0.27	−0.24	E5	1.60	11.00	22.37	36.18
E6	−0.32	−0.30	−0.28	−0.24	E6	6.63	16.75	30.00	30.50
E7	−0.35	−0.31	−0.29	−0.25	E7	10.18	21.00	27.39	28.50

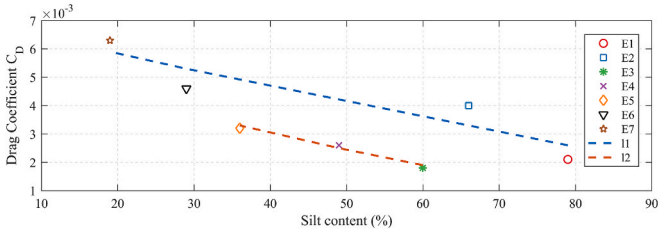

Fig. 7. Drag coefficient C_D of flat bed (scattered dots) over sediments E1-E7. C_D data of sediments E1, E2, E6 and E7 are roughly on line blue dashed l1, and those of E3, E4 and E5 are nearly on red dashed line l2. (For interpretation of the references to colour in this figure legend, the reader is referred to the web version of this article.)

2006; Rusello et al., 2006; Taylor, 1997), the expected uncertainty in C_D is considered under 12 %. The data points of E1, E2, E6, E7 and E3, E4, E5 are approximately on the parallel line $l1$ and $l2$, respectively. For both of the two lines, C_D decrease roughly linear with p_{silt}, suggesting that the increase of silt content can smoothen bed surface. However, $l2$ lies below $l1$, implying that the bed surface with p_{silt} of 36–60 % are relatively smoother than either silt- or sand-dominated beds. This phenomenon can be explained by two mechanisms. First, in more diversely composed sediment beds, fine particles fill the gaps between larger particles, leading to a smoother bed surface, reduced near-bed friction, and consequently higher time-averaged near-bed velocities. Second, the greater grain size nonuniformity in these beds increases the hiding-exposure effect, which suppresses the initiation of particle movement once the bed shear stress exceeds τ_{cr}, helping maintain the initial smoothness of the bed surface, thereby keeping C_D low. Consequently, the time-averaged near-bed velocity is increased.

At velocity levels 7 and 8 (with τ_b of 0.51–0.70 Pa), the equilibrium SSCs of sediment beds E3-E5 are smaller, indicating their stronger bed stability. At this stage, the sediment particles have already started in motion, yet the SSC of sediment beds E3-E5 are under 10 g/L and the ripples are not fully developed. Therefore, the composition of the surface layer is considered largely unchanged. Aside from reduced surface friction, two additional factors contribute to the reinforcement of inner bed structure, enhancing bed stability: Fine particles can more densely fill the interspace of the coarse particles, weakening seepage flow; reciprocally, the coarse particles can shelter the fine from being exposed to the surface flow. When the silt content is less than 36 %, coarse-grained sand predominates, increasing the interparticle voids and promoting seepage (Bartzke et al., 2013; Bartzke et al., 2017), which reduces the stability of the bed. When the silt content is greater than 60 %, fine-grained silt predominates. Due to the lack of coarse particles for sheltering, the silt is directly exposed to current, making the sediment particles more prone to suspension. Hence, the sediment beds with p_{silt} of 36 %-60 % have smaller SSC increments, and the distribution of SSCs follows the same feature.

However, as current velocity further increases, sediment particles are substantially suspended at velocity level 9 and above ($\tau_b \geq 1.00$ Pa), and the bed structure's resistance to erosion is largely overwhelmed. In this case, large amounts of fine sediment are eroded and suspended, leaving coarse-grained sediment at bed forming ripples (see Table 3). Compared to a flat bed, ripples create greater roughness, which enhances near-bed turbulence and promotes sediment suspension. Additionally, the hiding-exposure effect at the surface of sediment bed no longer stands, exposing the sublayer directly to current, making grain size become the decisive factor for SSC increment. Due to the linear correlation between silt content and grain size (as shown in Yao et al., 2022a), SSC increment is positively related to silt content, making equilibrium SSC and silt content quasi-linearly related. However, even if sediment structure cannot change the amount of sediment suspended under these conditions, it can still influence the suspension process duration (Fig. 4). Although the inner structure is intruded, sediment beds with greater nonuniformity have smaller porosity, impairing seepage flow and extending the erosion

time scale. For instance, the SSC development period for sediment beds E3-E5 remains longer at velocity levels 9–10.

4.2. Estimation of SSC at steady state

According to the results, the SSC of silt-dominated sediment can reach equilibrium under steady current conditions, suggesting a sand-like behaviour. Therefore, the concept of reference concentration—representing the near-bed equilibrium SSC—remains physically meaningful and applicable. Accurately predicting near-bed SSC is critical for simulating sediment transport in fine sediment-dominated tidal flat regions, as it reflects the maximum sediment supply capacity of the bed under equilibrium conditions. Meanwhile, as a key factor governing sediment suspension behaviour, the influence of silt content should be considered in the formulation.

Existing studies on the reference SSC of silty sediment mainly focus on wave conditions. Based on the formula proposed by van Rijn (2007b, hereinafter vR07), originally intended for the suspension behaviour of noncohesive sand (60–200 μm), Yao et al. (2015) modified the β coefficient in the vR07 formulation and extended its application to silt under wave conditions. In this study, we adopt the rationale of Yao et al. (2015) and modify the vR07 formulation to describe the relationship between SSC and bed shear stress for silt-dominated sediment under steady currents:

$$c_a = \beta\left(1 - p_{clay}\right) f_{silt} \frac{D_{50} T^{1.5}}{a D_*^{0.3}} = \beta c_{vR} \tag{3}$$

where c_a is the reference concentration by volume; c_{vR} is an empirical formulation; β is an empirical coefficient, which was suggested as 0.015 by van Rijn (2007b); p_{clay} is the clay content in sediment; D_{50} is the median grain size of the bed mixtures; f_{silt} is the silt factor, if $D_{50} > D_{sand} = 62\mu m$, $f_{silt} = 1$, else $f_{silt} = D_{sand}/D_{50}$; D_* is the dimensionless particle size, $D_* = D_{50}[(s-1)g/\nu^2]^{1/3}$, ν is the kinematic viscosity of water; a is the reference level (taken as 1 cm above bed in this study); T is the excess shear stress, $T = (\tau_b - \tau_{cr})/\tau_{cr}$, with τ_b being the bed shear stress and τ_{cr} the critical bed shear stress, taken as the calculated value of bed shear stress at the moment when abrupt change of SSC appeared in the experiment (Yao et al., 2022a, see Table 1).

As indicated by the experimental results, c_a does not necessarily increase with shear stress, but the depth-averaged SSC ($\overline{c}$) does, reflecting the unique flow characteristics in the annular flume. Due to the strong vertical mixing generated by the annular flume, the depth-averaged $\overline{c}$ retains significant near-bed features despite being a depth-averaged value. Thereby, it can be reasonably used as a representative parameter for equilibrium SSC, without contradicting the physical essence of the reference concentration.

Since the flow regime in the annular flume deviates from that of open-channel flow, the applicability of the commonly assumed exponent of 1.5 for excess shear stress (T) in eq. (3) is questionable under annular flume conditions, which requires further evaluation. Following Yao et al. (2015), an empirical parameter $c_{vR,1}$, which incorporates the contributions of sediment composition, grain size, and hydrodynamic force, is established, which is proportional to T:

$$c_{vR,1} = \left(1 - p_{clay}\right) f_{silt} \frac{D_{50} T}{a D_*^{0.3}} \tag{4}$$

Owing to the bed shear stress (τ_b) recorded by ADV affected greatly by the SSC, the τ_b in T is taken as the bed shear stress in clean water condition, as shown in Table 2. The scattered $\overline{c}$-$c_{vR,1}$ data points for sediments E1-E6 are plotted on a base-10 log–log scale in Fig. 8 (excluding E7 for too few valid data), with y-axis and x-axis representing $\overline{c}$ (in volume) and $c_{vR,1}$, respectively. As shown in Fig. 8, the power-law trends fitted for each sediment are represented by dashed lines, which are nearly parallel, with slopes close to 2. This suggests that, for the flow

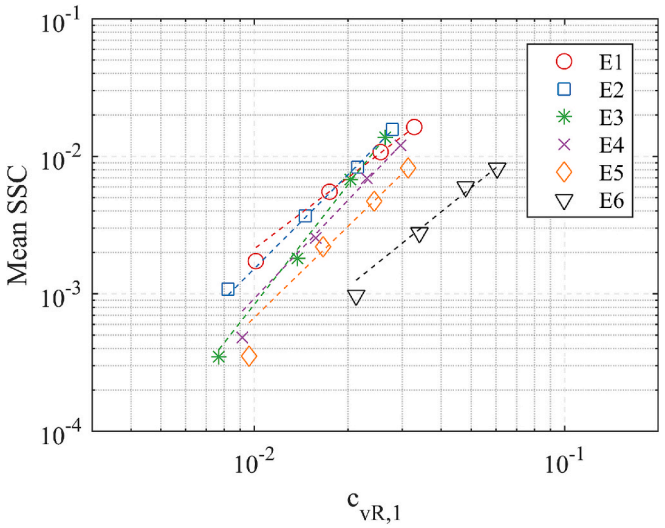

Fig. 8. The relationship between mean volume SSC $\overline{c}$ and empirical parameter $c_{vR,1} = \left(1 - p_{clay}\right) f_{silt} \frac{D_{50} T}{a D_*^{0.3}}$, the T-exponents (gradients of the fitted lines) of E1-E6 are 1.71, 2.27, 2.88, 2.37, 2.20 1.82, respectively. E7 is excluded from the plot since it only has two valid data points.

regime in the annular flume, $\overline{c}$ is proportional to T^2, rather than to $T^{1.5}$ as suggested by vR07.

According to Yao et al. (2022a), when silt content (p_{silt}) exceeds 35 %, the enhancing effect of silty bed structure on τ_{cr} should be considered. For sediment suspension to occur, bed shear stress τ_b needs to overcome the τ_{cr} of structured sediment bed. Once this threshold is surpassed, the sediment particles behave as discrete particles rather than as part of a structured bed. In such cases, the portion of τ_b overcoming τ_{cr} acts on discrete particles and should be normalised by the critical shear stress of individual particles $\tau_{cr,o}$. Therefore, for sediments with p_{silt} over 35 %, the excess shear stress of sediment is modified as:

$$T_m = \begin{cases} T & \text{for } p_{silt} < 35\% \\ \dfrac{\tau_{cr}}{\tau_{cr,o}} T & \text{for } p_{silt} \geq 35\% \end{cases} \tag{5}$$

This modification does not change the power-law relationship between T_m and $\overline{c}$ with an exponent of 2. To facilitate the analysis of the relationship between $\overline{c}$ and the modified excess shear stress T_m, an empirical variable $c_{vR,2}$ is introduced, which incorporates the square of T_m:

$$c_{vR,2} = \left(1 - p_{clay}\right) f_{silt} \frac{D_{50} T_m^2}{a D_*^{0.3}} \tag{6}$$

Fig. 9 illustrates the relationship between $\overline{c}$ and $c_{vR,2}$, and the fitted line of the data for all sediments is indicated with a single line. The gradient of the fitted line happens to be $\beta = 0.015$, which is in line with the value suggested by vR07 for sand. To sum up, the depth-averaged SSC of silty sediment contributed by the flow in annular flume can be estimated by:

$$\overline{c} = 0.015\left(1 - p_{clay}\right) f_{silt} \frac{D_{50} T_m^2}{a D_*^{0.3}} \tag{7}$$

This formula is applicable to flow in annular flume condition. It is worth noting that both Eq. (3) and Eq. (7) can be applied to sediment beds E6 and E7, meanwhile $T_m = T$ for these two types of sediments, so the only difference between depth-averaged SSC $\overline{c}$ in annular flume and reference concentration c_a in open channel is the exponent of the excess shear stress, which can be attributed to the difference between open-channel and annular flume flow conditions. Hence, this correlation suggests that while Eq. (7) is derived for the flow in an annular flume, it can be

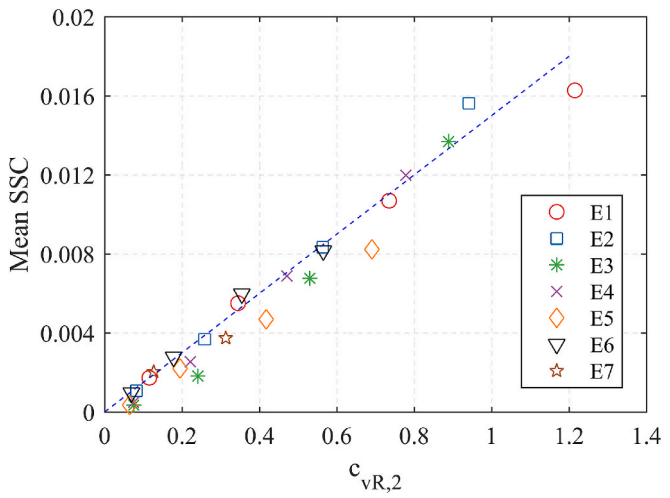

Fig. 9. The relationship between depth-averaged SSC $\bar{c}$ and empirical parameter $c_{vR,2} = \left(1 - p_{clay}\right) f_{silt} \frac{D_{50} T_m^2}{a D_*^{0.3}}$, the gradient of the fitted line is 0.015, with valid data points of E7 at velocity levels 7 and 8 included.

also applied for predicting the reference concentration in open channel flow, which requires further validation. The present study is primarily concerned with establishing the formulation under controlled laboratory conditions. Further validation against field data is necessary and is an important direction for future research.

4.3. Experiment inspired numerical modelling on silt erosion under current

As is illustrated in Fig. 4, under steady current, the SSC of silt-dominated sediment experienced a developing process before reaching equilibrium. To predict the development process of SSC for silt-dominated sediment, we neglect the differences in the streamwise and transverse directions within the annular flume. Thus, the 1-D advection–diffusion equation is utilized:

$$\frac{\partial c}{\partial t} = \frac{\partial}{\partial z} \varepsilon_s \frac{\partial c}{\partial z} + w_s \frac{\partial c}{\partial z} \tag{8}$$

where, c is the SSC; w_s is the settling velocity; ε_s is the sediment mixing coefficient. Before the start of computation, the initial SSC profile and the equilibrium reference concentration should be prescribed. The initial SSC profile at certain velocity level is taken as the steady SSC profile of the previous velocity level; the equilibrium reference concentration is taken as the value at the elevation of 1 cm in the SSC profile of the current velocity level (as listed in Table 4). Specially, for the initial SSC profiles of suspension processes at velocity level 7, although the measured data of steady SSC distributions at velocity level 6 are unavailable, the profiles can be derived from the initial values of SSC series converted from the recorded IBS signals at various elevations. At equilibrium state, Eq. (8) is reduced to:

$$\varepsilon_s \partial c / \partial z + w_s c = 0 \tag{9}$$

The settling velocity of suspended sediment w_s is calculated according to van Rijn (2007b) using grain size provided in Supplementary Material Table 2. Combined with Eq. (9) and the fitting result shown in Table 4, the mixing coefficient ε_s is therefore determined.

At the water surface, net sediment flux is assumed to be zero, described by:

$$\varepsilon_s \partial c / \partial z + w_s c = 0 \; at \; z = h \tag{10}$$

For the bed boundary condition, there are two common types: type I, concentration condition (Eq. 11), which assumes the concentration at the reference level to be the equilibrium value c_a:

$$c = c_a \quad at \; z = z_a \tag{11}$$

Type II, gradient condition (Eq. 12), which presumes a constant upward sediment flux:

$$-\varepsilon_s \partial \mathrm{c} / \partial \mathrm{z} = w_s c_a \quad at \; z = z_a \tag{12}$$

Based on type II condition, we propose a new boundary condition (type III) which prescribes the upward sediment flux to be asymptotically approaching the equilibrium value, referred to as the asymptotic flux:

$$-\varepsilon_s \partial \mathrm{c} / \partial \mathrm{z} = w_s [\alpha c_a + (1 - \alpha) c] \; at \; z = z_a \tag{13}$$

The relaxation coefficient α indicates the development pattern of upward flux: when $0 < \alpha < 1$, the upward flux at start is smaller than that of the steady state, and increases gradually to approach equilibrium; when $\alpha > 1$, the initial upward flux is initially larger than the equilibrium value, and reduces gradually to steady state; when $\alpha = 1$, type III turns into type II, the upward flux keeps as a constant. The three types of bed boundary conditions are respectively applied to the same representative case of sediment E6 at velocity level 8, each yielding a time series of SSC development.

Fig. 10a shows the numerical and experimental depth-averaged SSC development curves for sediment bed E6 at velocity level 8, while the corresponding SSC profiles at 0, 100, 200, 400, 600, 800, 1000, and 1200 s after the initiation of the suspension process are presented in Fig. 10b. Compared with the experimental results, the numerical results using Type I and Type II boundary conditions exhibit a much faster progression, reaching equilibrium by approximately 200 s and 400 s, respectively. But the experimental results indicate that the equilibrium SSC is not achieved until around 1200 s. At the onset of suspension, the upward sediment flux does not immediately reach equilibrium. Instead, it initially increases to an intermediate value between the pre-suspension upward flux and the equilibrium value, then gradually approaches equilibrium over time. Only the numerical results using the Type III boundary condition ($\alpha = 0.13$) closely replicate the suspension process, with the mean SSC development curve and profile evolution aligning well with the experimental data. This suggests that the Type III boundary condition effectively captures the underlying physical mechanisms of silty sediment suspension.

In fact, both experimental results and Type III bed boundary conditions indicate a delayed erosion processes over silty bed. Combining the experimental results analysis and the numerical simulation, we propose the following mechanism related to the suspension of silty bed: In silty beds, sediment exists in the form of a network structure (silt-skeleton), where sediment particles are bound together by structural force, as mentioned by Yao et al. (2022a). When the shear stress exceeds the erosion threshold of the sediment bed, erosion begins, causing particles in the surface layer to gradually detach from the network structure and become suspended. However, the breakdown of the network structure is a gradual process. As erosion progresses, surface particles transition from being part of the skeleton to existing as discrete particles. This results in a continuous increase in the upward sediment flux until equilibrium is achieved, at which point the erosion depth of the sediment bed reaches its maximum. However, it is worth noting that Eq. 8 suggests that the time derivative of SSC is contributed by both upward flux and settling flux, therefore the settling velocity w_s also plays an important role in suspension process. Understanding the contribution of w_s requires further investigation in future studies.

4.4. Suspension time scale and the relevant factors of influence

As shown in Figs. 4 and 10, the time required for SSC to reach equilibrium varies significantly across different sediment types and current conditions. To investigate the factors influencing the suspension process, it is essential to quantify its duration. By fitting the normalized

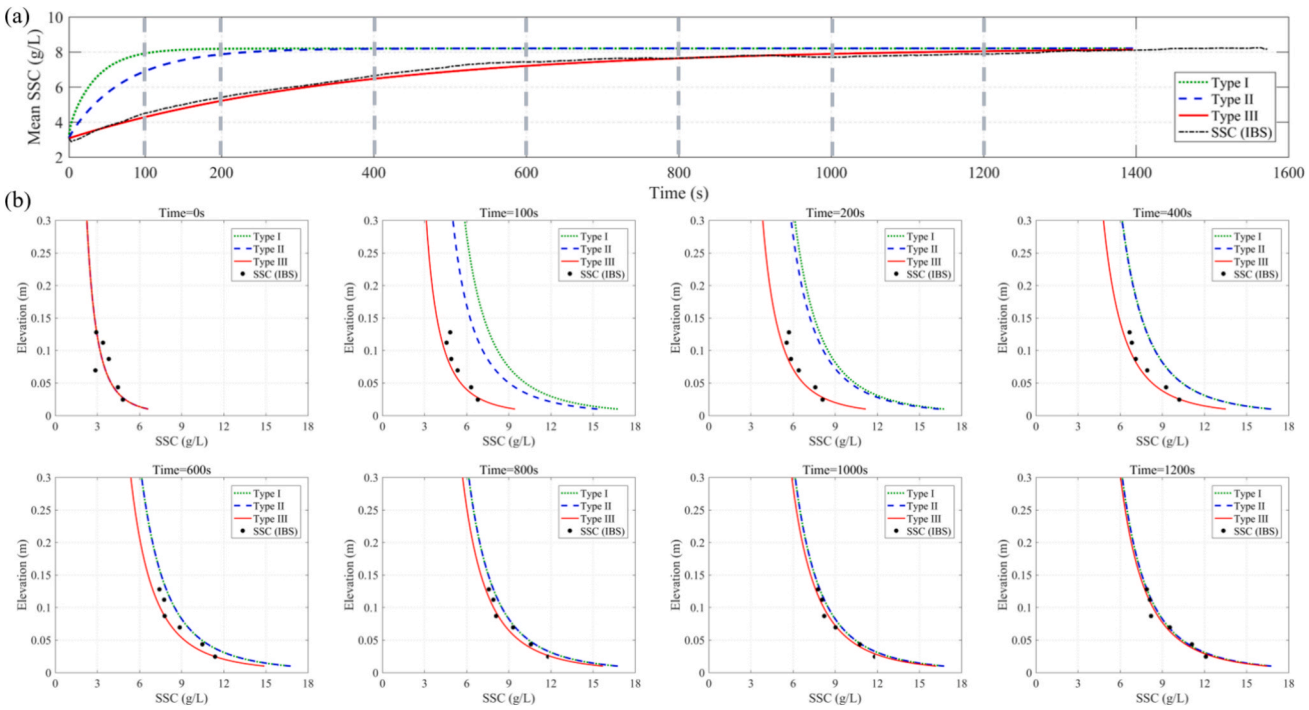

Fig. 10. (a) Numerical and experimental mean SSC development curves for sediment E6 at velocity level 8. The numerical results using Type I, Type II, and Type III boundary conditions are represented by the green dotted line, blue dashed line, and red solid line, respectively. The experimental mean SSC time series, converted from IBS signals, is shown by the black dash-dot line. (b) SSC profiles from numerical results and experimental data at 0, 100, 200, 400, 600, 800, 1000, and 1200 s after the initiation of the suspension process. Numerical results use the same line styles as in (a), while experimental SSC data, converted from IBS signals, are shown only at the elevations corresponding to IBS installations, indicated by black solid dots. (For interpretation of the references to colour in this figure legend, the reader is referred to the web version of this article.)

SSC increment with an exponential function, we propose a time scale (t_A) to represent the duration of the suspension process:

$$\Delta C_n = (\overline{c}(t) - \overline{c_0})/(\overline{c_e} - \overline{c_0}) = 1 - exp(-t/t_A) \quad (14)$$

in which $\overline{c}(t)$ is the depth-averaged concentration as the function of time; $\overline{c_0}$ and $\overline{c_e}$ are the depth-averaged initial and equilibrium concentration, $\overline{c_0} = \overline{c}(0)$, and ΔC_n is the normalised SSC increment, with $\Delta C_n(0) = 0$ and $\Delta C_n(t \to \infty) = 1$; t_A is the suspension time scale required to reach equilibrium, which reflects the bed structure's ability to delay the progression of erosion.

The comparison of fitted (solid) and original (dotted) curves is illustrated in Fig. 11, and the fitted results of t_A for suspension processes at velocity levels 7–10 for different sediments are shown in Fig. 12. As current velocity increases, t_A exhibits contrasting trends depending on sediment composition. For sediment beds E1, E2, E6 and E7, t_A decreases, which indicates that for beds predominantly composed of silt or sand, they can only delay the erosion under low shear stress. However, as shear stress further rises, this delaying ability diminishes. While for sediment beds E3, E4, and E5, t_A increases with the rise of current velocity, particularly at velocity levels 9 and 10, where their t_A values are significantly larger than the others. It is noted that the t_A is rather small for Sediment E3 at velocity level 7. Based on the observations and measured SSC, the flow velocity at level 7 induced only minimal surface erosion on the Sediment E3. Constrained by sediment availability, the steady SSC can be achieved very rapidly.

Since the hydrodynamic conditions were the same for all sediment beds, the aforementioned contrasting behaviour of t_A is believed to be attributed to bed composition, which can be represented by the grain size nonuniformity, i.e., D_{90}/D_{10}. As shown in Table 1, the sediment beds E3–E5, which are more diversely composed, have higher D_{90}/D_{10} values compared to the other sediments. This larger grain size diversity contributes to their more compact bed structure, leading to their stronger ability to delay erosion with the rise of shear stress. However, this buildup in erosion resistance is not unlimited. For example, t_A for sediment bed E4 at velocity level 10 dropped by half after peaking at velocity level 9, suggesting that this delaying ability may decline under more intense current conditions.

On the silty tidal flats, such as the Jiangsu coast tidal flat, a phase lag (characterized by h/w_s) between sediment suspension and flow velocity was frequently observed (Gong et al., 2017; Zhang et al., 2016). This lag describes the time delay between the peak current and the maximum SSC due to small settling velocities of fine-grained sediments. The suspension time scale identified in this study provides an additional mechanism for this phenomenon on the silty tidal flat. That is, under steady flow currents, a certain period is required for the equilibrium SSC development of near bed region. The delay of near bed equilibrium SSC development would further postpone the peak SSC over the whole water column. That is, the time lag of sediment suspension over silty bed can be controlled by both settling velocity and unsteady upward flux (i.e., Eq. 13). As a result, considering the periodical variations of tidal currents, the sediment transport rate may further lag behind the flow intensity, highlighting the extra consideration on modelling sediment transport over silty bed.

5. Conclusions

This study has conducted a series of erosion experiments in an annular flume, to explore suspended sediment dynamics over different sand-silt mixtures. In total, seven different sand-silt mixtures with silt contents ranging from 19 %-79 % were tested. These experiments lead to the following conclusions.

Under steady current conditions, the SSC of sand-silt mixtures gradually increases, eventually reaching equilibrium. Sediment beds with 36–60 % silt content exhibit higher mean velocities, lower equilibrium SSCs, and prolonged SSC development due to their poorly graded nature. The larger nonuniformity in gradation contributes to the

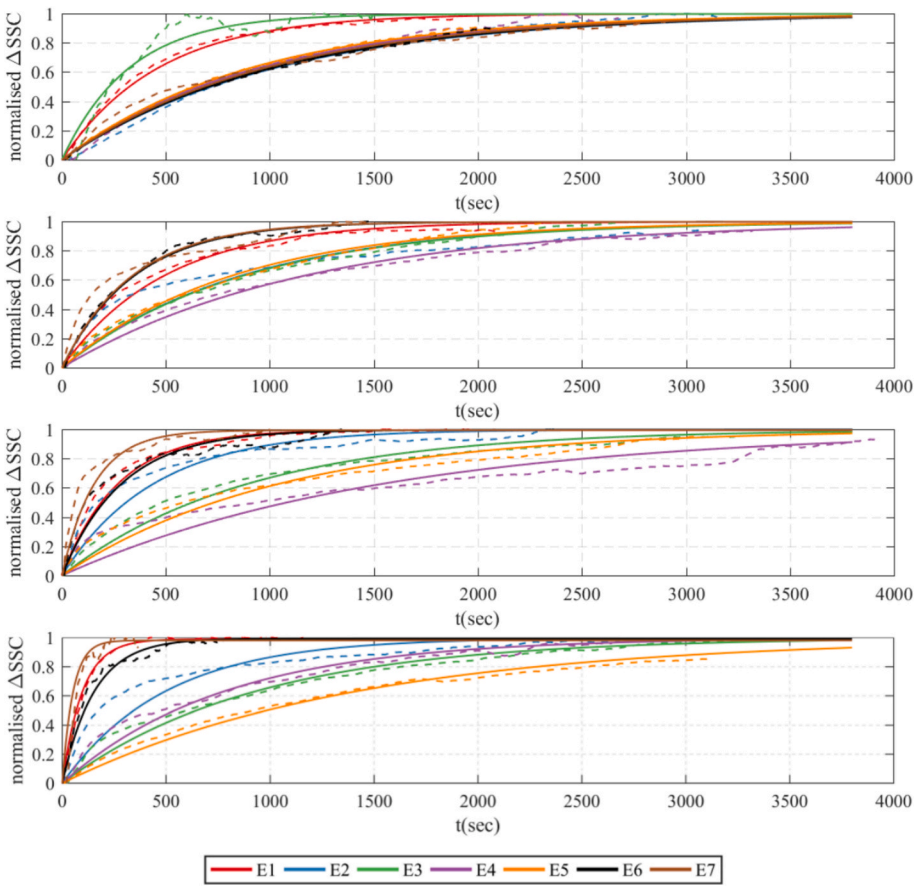

Fig. 11. Comparisons between fitted curves (solid) and curves of experiment data (dashed) of mean SSC development. The fitted and experiment curves of the same sediment sample are in the same colour.

t_A (s)	7th	8th	9th	10th
E1	466	494	271	96
E2	1035	868	444	496
E3	325	877	903	931
E4	952	1175	1561	780
E5	915	823	1056	1418
E6	1020	349	288	153
E7	985	340	156	51

Fig. 12. Fitted results of suspension time scale t_A for suspension processes at velocity levels 7–10 for different sediments.

reduced bed friction and enhanced stability, resulting in higher mean velocities and smaller equilibrium SSCs. However, when bed shear stress overwhelms bed resistance, these advantages diminish, but the prolonged SSC development process becomes more prominent.

Building on this observation, the vR07 formula was recalibrated to predict the equilibrium concentration of silty sediment under current conditions. The equilibrium SSC, represented by depth-averaged SSC, was found to be proportional to the square of the excess shear stress. After modifying the excess shear stress for sediment beds with more than 35 % silt content, it was found that the equilibrium SSC for sediment beds with silt content ranging from 19 % to 79 % can be predicted using a unified formula. Although the formula proposed in this study is specific to the flow in an annular flume, it can be also applied for predicting the reference concentration in open channel flow, which requires further validation.

To advance the modelling of sediment suspension, we examined boundary conditions governing the suspension process. Two commonly used bottom boundary conditions were considered: the concentration

type, which prescribes a reference concentration, and the gradient type, which specifies a constant upward sediment flux. Based on the gradient type, a novel boundary condition has been introduced by prescribing a developing upward sediment flux towards equilibrium, referred to as the asymptotic flux condition. This new condition has been demonstrated to be the most practical and effective among the three.

Furthermore, we investigated the development process of SSC towards equilibrium, which can be represented by a time scale (t_A). This suspension time scale was determined by fitting SSC development curves. As velocity increases, t_A decreases for silt- or sand-predominated beds, while it increases for more diversely composed sediments. Higher nonuniformity in grain size enhances the strength of bed structure, promoting the ability of delaying erosion, though this ability diminishes under higher shear stress.

CRediT authorship contribution statement

Zhongxing Qiao: Writing – original draft, Formal analysis. **Yongping Chen:** Supervision, Methodology, Conceptualization. **Peng Yao:** Writing – review & editing, Writing – original draft, Supervision, Methodology, Conceptualization. **Min Su:** Methodology, Formal analysis. **Marcel Stive:** Writing – review & editing, Visualization, Conceptualization. **Lei Ren:** Writing – review & editing, Formal analysis. **Zhengbing Wang:** Writing – review & editing, Supervision, Conceptualization.

Declaration of competing interest

The authors declare that they have no known competing financial interests or personal relationships that could have appeared to influence the work reported in this paper.

Acknowledgements

This work is funded by National Key R&D Program of China (Grant No. 2022YFC3106201), National Natural Science Foundation of China (Grant No. 42476166, 51620105005), the Open Fund of Key Laboratory of Ocean Space Resource Management Technology, MNR, China (Grant No. KF-2023-106), Natural Resources Science and Technology Innovation Project of Jiangsu Province (Grant No. JSZRKJ202402) and the Belt and Road Special Foundation of the National Key Laboratory of Water Disaster Prevention (Grant No. 2022491711).

Appendix A. Supplementary data

Supplementary data to this article can be found online at https://doi.org/10.1016/j.jhydrol.2025.133836.

Data availability

Data will be made available on request.

References

Aberle, J., Nikora, V., Walters, R., 2004. Effects of bed material properties on cohesive sediment erosion. Mar. Geol. 207, 83–93. https://doi.org/10.1016/j.margeo.2004.03.012.

Banasiak, R., Verhoeven, R., 2008. Transport of sand and partly cohesive sediments in a circular pipe run partially full. J. Hydraul. Eng. 134, 216–224. https://doi.org/10.1061/(ASCE)0733-9429(2008)134:2(216).

Bartzke, G., Bryan, K., Pilditch, C., Huhn, K., 2013. On the stabilizing influence of silt on sand beds. J. Sediment. Res. 83, 691–703. https://doi.org/10.2110/jsr.2013.57.

Bartzke, G., Huhn, K., Bryan, K.R., 2017. A computational investigation of the interstitial flow induced by a variably thick blanket of very fine sand covering a coarse sand bed. Geo-Mar. Lett. 37, 457–474. https://doi.org/10.1007/s00367-017-0502-x.

Berlamont, J., Ockenden, M., Toorman, E., Winterwerp, J., 1993. The characterisation of cohesive sediment properties. Coast. Eng. 21, 105–128. https://doi.org/10.1016/0378-3839(93)90047-C.

Blanckaert, K., Lemmin, U., 2006. Means of noise reduction in acoustic turbulence measurements. J. Hydraul. Res. 44 (1), 3–17. https://doi.org/10.1080/00221686.2006.9521657.

Booij, R., Tukker, J., 1996. 3-dimensional laser-Doppler measurements in a curved flume. In: Developments in Laser Techniques and Applications to Fluid Mechanics. Springer Berlin Heidelberg, Berlin, Heidelberg, pp. 98–114.

Cao, Z., 1997. Turbulent bursting-based sediment entrainment function. J. Hydraul. Eng. 123, 233–236. https://doi.org/10.1061/(ASCE)0733-9429(1997)123:3(233).

Celik, I., Rodi, W., 1988. Modeling suspended sediment transport in nonequilibrium dituations. J. Hydraul. Eng. 114, 1157–1191. https://doi.org/10.1061/(ASCE)0733-9429(1988)114:10(1157).

Chen, D., Melville, B., Zheng, J., Wang, Y., Zhang, C., Guan, D., Chen, C., 2021a. Pickup rate of non-cohesive sediments in low-velocity flows. J. Hydraul. Res. 60 (1), 125–135. https://doi.org/10.1080/00221686.2020.1871430.

Chen, D., Wang, Y., Melville, B., Huang, H., Zhang, W., 2018. Unified formula for critical shear stress for erosion of sand, mud, and sand–mud mixtures. J. Hydraul. Eng. 144, 04018046. https://doi.org/10.1061/(ASCE)HY.1943-7900.0001489.

Chen, D., Zheng, J., Zhang, C., Guan, D., Li, Y., Huang, H., 2022. Threshold of surface erosion of cohesive sediments. Front. Mar. Sci. 9, 847985.

Chen, Y., Qiao, Z., Xu, C., Yao, P., 2021b. Influences of sediment composition on scour of silt-sand mixture bed. J. Sedim. Res. 46, 1–8. https://doi.org/10.16239/j.cnki.0468-155x.2021.05.001.

de Leeuw, J., Lamb, M.P., Parker, G., Moodie, A.J., Haught, D., Venditti, J.G., Nittrouer, J.A., 2020. Entrainment and suspension of sand and gravel. Earth Surf. Dyn. 8, 485–504. https://doi.org/10.5194/esurf-8-485-2020.

Dinehart, R.L., Burau, J.R., 2005. Repeated surveys by acoustic Doppler current profiler for flow and sediment dynamics in a tidal river. J. Hydrol. 314, 1–21. https://doi.org/10.1016/j.jhydrol.2005.03.019.

Diplas, P., Dancey, C.L., Celik, A.O., Valyrakis, M., Greer, K., Akar, T., 2008. The role of impulse on the initiation of particle movement under turbulent flow conditions. Science 322, 717–720. https://doi.org/10.1126/science.1158954.

Dong, P., 2007. Two-fraction formulation of critical shear stresses for sand and silt mixtures. J. Waterw. Port Coast. Ocean Eng. 133, 238–241. https://doi.org/10.1061/(ASCE)0733-950X(2007)133:3(238).

Egiazaroff, I.V., 1965. Calculation of nonuniform sediment concentrations. J. Hydraul. Div. 91, 225–247. https://doi.org/10.1061/JYCEAJ.0001277.

Einstein, H.A., 1950. The bedload function for sediment transportation in open channel flows. Tech. Bulletin No. 1026.

Engelund, F., Fredsøe, J., 1976. A sediment transport model for straight alluvial channels. Hydrol. Res. 7, 293–306.

Gailani, J., Jin, L., McNeil, J., Lick, W., 2001. Effects of bentonite clay on sediment erosion rates. DOER Technical Notes Collection (ERDC TN-DOER-N9), U.S. Army Engineer Research and Development Center, Vicksburg, MS.

Gao, S., 2019. Chapter 10 - Geomorphology and sedimentology of tidal flats, in: Perillo, G.M.E., Wolanski, E., Cahoon, D.R., Hopkinson, C.S. (Eds.), Coastal Wetlands (Second Edition). Elsevier, pp. 359–381. Doi: 10.1016/B978-0-444-63893-9.00010-1.

García, M., Parker, G., 1991. Entrainment of bed sediment into suspension. J. Hydraul. Eng.-Asce 117. https://doi.org/10.1061/(ASCE)0733-9429(1991)117:4(414).

Gong, Z., Jin, C., Zhang, C., Zhou, Z., Zhang, Q., Li, H., 2017. Temporal and spatial morphological variations along a cross-shore intertidal profile, Jiangsu, China. Cont. Shelf Res. 144, 1–9. https://doi.org/10.1016/j.csr.2017.06.009.

Goring, D.G., Nikora, V.I., 2002. Despiking acoustic Doppler velocimeter data. J. Hydraul. Eng. 128, 117–126. https://doi.org/10.1061/(ASCE)0733-9429(2002)128:1(117).

Houwing, E.-J., 2000. Morphodynamic development of intertidal mudflats: consequences for the extension of the pioneer zone. Cont. Shelf Res. 20, 1735–1748. https://doi.org/10.1016/S0278-4343(00)00045-5.

Hu, P., Ji, A., Li, W., Tang, X., Xiao, W., Cao, Z., 2025. Capacity and noncapacity sediment transport characteristics in the overtopping-induced dam-breaching process. J. Hydraul. Eng. 151, 04025001. https://doi.org/10.1061/JHEND8.HYENG-13985.

Hu, P., Tan, L., He, Z., 2020. Numerical investigation on the adaptation of dam-break flow-induced bed load transport to the capacity regime over a sloping bed. J. Coast. Res. 36, 1237–1246. https://doi.org/10.2112/JCOASTRES-D-19-00120.1.

Jacobs, W., Le Hir, P., Van Kesteren, W., Cann, P., 2011. Erosion threshold of sand–mud mixtures. Cont. Shelf Res. 31, S14–S25. https://doi.org/10.1016/j.csr.2010.05.012.

Jia, Y., Liu, X., Zhang, S., Shan, H., Zheng, J., 2020. Wave-forced sediment Erosion and Resuspension in the Yellow River Delta. Doi: 10.1007/978-981-13-7032-8.

Kuai, Y., Tao, J., Zhou, Z., Aarninkhof, S., Wang, Z.B., 2021. Sediment characteristics and intertidal beach slopes along the Jiangsu Coast, China. J. Mar. Sci. Eng. 9. https://doi.org/10.3390/jmse9030347.

Mastbergen, D., Berg, J.H., 2003. Breaching in fine sands and the generation of sustained turbidity currents in submarine canyons. Sedimentology 50. https://doi.org/10.1046/j.1365-3091.2003.00554.x.

McLean, S.R., 1992. On the calculation of suspended load for noncohesive sediments. J. Geophys. Res. Oceans 97, 5759–5770. https://doi.org/10.1029/91JC02933.

Mehta, Partheniades, 1982. Resuspension of deposited cohesive sediment beds. Coast. Eng. 1982, 1569–1588.

Meyer-Peter, E., Muller, R., 1948. Formulas for bed load transport. Proceedings of 2nd meeting of the International Association for Hydraulic Structures Research, Delft, June 7, 1948, pp. 39–64.

Mitchener, H., Torfs, H., 1996. Erosion of mud/sand mixtures. Coast. Eng. 29, 1–25. https://doi.org/10.1016/S0378-3839(96)00002-6.

Murray, W.A., 1976. Erodibility of coarse sand/clayey silt mixtures. Lehigh University.

Panagiotopoulos, I., Voulgaris, G., Collins, M.B., 1997. The influence of clay on the threshold of movement of fine sandy beds. Coast. Eng. 32, 19–43. https://doi.org/10.1016/S0378-3839(97)00013-6.
Parchure, T.M., Mehta, A.J., 1985. Erosion of soft cohesive sediment deposits. J. Hydraul. Eng. 111, 1308–1326. https://doi.org/10.1061/(ASCE)0733-9429(1985)111:10(1308).
Perera, C., Smith, J., Wu, W., Perkey, D., Priestas, A., 2020. Erosion rate of sand and mud mixtures. Int. J. Sedim. Res. 35, 563–575. https://doi.org/10.1016/j.ijsrc.2020.06.004.
Perkey, D., Smith, S.J., Priestas, A., 2020. Erosion thresholds and rates for sand-mud mixtures. U.S. Army Engineer Research and Development Center.
Pope, N.D., Widdows, J., Brinsley, M.D., 2006. Estimation of bed shear stress using the turbulent kinetic energy approach—A comparison of annular flume and field data. Cont. Shelf Res. 26, 959–970. https://doi.org/10.1016/j.csr.2006.02.010.
Reed, C.W., Niedoroda, A.W., Swift, D.J.P., 1999. Modeling sediment entrainment and transport processes limited by bed armoring. Mar. Geol. 154, 143–154. https://doi.org/10.1016/S0025-3227(98)00109-1.
Roberts, J., Jepsen, R., Gotthard, D., Lick, W., 1998. Effects of particle size and bulk density on erosion of quartz particles. J. Hydraul. Eng. 124, 1261–1267. https://doi.org/10.1061/(ASCE)0733-9429(1998)124:12(1261).
Rusello, P.J., Lohrmann, A., Siegel, E., Maddux, T., 2006. Improvements in acoustic Doppler velocimetry. Proceedings of the Seventh International Conference on Hydroscience and Engineering.
Sanford, L.P., Maa, J.-P.-Y., 2001. A unified erosion formulation for fine sediments. Mar. Geol. 179, 9–23. https://doi.org/10.1016/S0025-3227(01)00201-8.
Shields, A., 1936. Anwendung der Ahnlichkeitsmechanik und der Turbulenzforschung auf die Geshchiebewefung. Versuchsanstalt fur Wasserbau und Schifbau.
Smith, J.D., McLean, S.R., 1977. Boundary layer adjustments to bottom topography and Suspended Sediment. Elsevier Oceanography Series. Elsevier 123–151. https://doi.org/10.1016/S0422-9894(08)70839-0.
Staudt, F., Mullarney, J.C., Pilditch, C.A., Huhn, K., 2019. Effects of grain-size distribution and shape on sediment bed stability, near-bed flow and bed microstructure. Earth Surf. Proc. Land. 44, 1100–1116. https://doi.org/10.1002/esp.4559.
Stone, M., Krishnappan, B.G., Emelko, M.B., 2008. The effect of bed age and shear stress on the particle morphology of eroded cohesive river sediment in an annular flume. Water Res. 42, 4179–4187. https://doi.org/10.1016/j.watres.2008.06.019.
te Slaa, S., He, Q., van Maren, D.S., Winterwerp, J.C., 2013. Sedimentation processes in silt-rich sediment systems. Ocean Dyn. 63, 399–421. https://doi.org/10.1007/s10236-013-0600-x.
te Slaa, S., van Maren, D.S., He, Q., Winterwerp, J.C., 2015. Hindered settling of silt. J. Hydraul. Eng. 141, 04015020. https://doi.org/10.1061/(ASCE)HY.1943-7900.0001038.
Taylor, J., 1997. Introduction to error analysis, the study of uncertainties in physical measurements.
Thompson, C.E.L., Amos, C.L., Lecouturier, M., Jones, T.E.R., 2004. Flow deceleration as a method of determining drag coefficient over roughened flat beds. J. Geophys. Res. Oceans 109. https://doi.org/10.1029/2001JC001262.
Torfs, H., 1995. Erosion of mud/sand mixtures. Katholieke Universiteit Leuven, Leuven.
van Ledden, M., van Kesteren, W.G.M., Winterwerp, J.C., 2004. A conceptual framework for the erosion behaviour of sand–mud mixtures. Cont. Shelf Res. 24, 1–11. https://doi.org/10.1016/j.csr.2003.09.002.
van Prooijen, B.C., Winterwerp, J.C., 2010. A stochastic formulation for erosion of cohesive sediments. J. Geophys. Res. Oceans 115. https://doi.org/10.1029/2008JC005189.
van Rhee, C., 2010. Sediment entrainment at high flow velocity. J. Hydraul. Eng. 136, 572–582. https://doi.org/10.1061/(ASCE)HY.1943-7900.0000214.
van Rijn, L.C., 2007a. Unified view of sediment transport by currents and waves. I: initiation of motion, bed roughness, and bed-loadtransport. J. Hydraul. Eng. 133, 649–667. https://doi.org/10.1061/(ASCE)0733-9429(2007)133:6(649).
van Rijn, L.C., 2007b. Unified View of Sediment Transport by Currents and Waves. II: Suspended Transport. J. Hydraul. Eng. 133, 668–689. https://doi.org/10.1061/(ASCE)0733-9429(2007)133:6(668).
van Rijn, L.C., 2020. Erodibility of mud–sand bed mixtures. J. Hydraul. Eng. 146, 04019050. https://doi.org/10.1061/(ASCE)HY.1943-7900.0001677.
van Rijn, L.C., 1984. Sediment transport, part II: suspended load transport. J. Hydraul. Eng. 110, 1613–1641. https://doi.org/10.1061/(ASCE)0733-9429(1984)110:11(1613).
Walder, J.S., 2016. Dimensionless erosion laws for cohesive sediment. J. Hydraul. Eng. 142, 04015047. https://doi.org/10.1061/(ASCE)HY.1943-7900.0001068.
Wang, Y., Zhu, D., 1990. Tidal flats of China. Quatern. Sci. 10, 291–300.
Wilcock, P.R., 1998. Two-fraction model of initial sediment motion in gravel-bed rivers. Science 280, 410–412. https://doi.org/10.1126/science.280.5362.410.
Winterwerp, J.C., 2001. Stratification effects by cohesive and noncohesive sediment. J. Geophys. Res. Oceans 1978–2012 (106), 22559–22574.
Winterwerp, J.C., van Kesteren, W.G.M., van Prooijen, B., Jacobs, W., 2012. A conceptual framework for shear flow–induced erosion of soft cohesive sediment beds. J. Geophys. Res. Oceans 117. https://doi.org/10.1029/2012JC008072.
Wright, S., Parker, G., 2004. Flow Resistance and suspended load in sand-bed rivers: Simplified stratification model. J. Hydraul. Eng. 130, 796–805. https://doi.org/10.1061/(ASCE)0733-9429(2004)130:8(796).
Xing, F., Wang, Y.P., Jia, J., 2022. Hydrodynamics and sediment transport patterns on intertidal flats along middle Jiangsu coast. Anthropocene Coasts 5, 12.
Yao, P., Hu, Z., Su, M., Chen, Y., Ou, Suying, 2018. Erosion behavior of sand-silt mixtures: the role of silt content. J. Coast. Res. 85, 1171–1175. https://doi.org/10.2112/SI85-235.1.
Yao, P., Su, M., Wang, Z., van Rijn, L.C., Stive, M.J.F., Xu, C., Chen, Y., 2022a. Erosion behavior of sand-silt mixtures: revisiting the erosion threshold. Water Resour. Res. 58, e2021WR031788. https://doi.org/10.1029/2021WR031788.
Yao, P., Su, M., Wang, Z., van Rijn, L.C., Zhang, C., Chen, Y., Stive, M.J.F., 2015. Experiment inspired numerical modeling of sediment concentration over sand–silt mixtures. Coast. Eng. 105, 75–89.
Yao, P., Sun, W., Guo, Q., Su, M., 2022b. Experimental study on the effect of sediment composition and water salinity on settling processes of quartz silt in still water. J. Sedim. Res. (in Chin.) 1–8. https://doi.org/10.16239/j.cnki.0468-155x.2022.05.003.
Zhang, Q., Gong, Z., Zhang, C., Townend, I., Jin, C., Li, H., 2016. Velocity and sediment surge: what do we see at times of very shallow water on intertidal mudflats? Cont. Shelf Res. 113, 10–20. https://doi.org/10.1016/j.csr.2015.12.003.
Zhang, Y., Xiao, X., Sun, Z., Lei, B., Li, M., Guo, X., Fu, T., Xing, C., 2024. Salt dynamic changes between seawater and phreatic brine in muddy tidal flats under tidal influence. J. Hydrol. 634, 131044. https://doi.org/10.1016/j.jhydrol.2024.131044.
Zhou, Z., Liu, Q., Fan, D., Coco, G., Gong, Z., Möller, I., Xu, F., Townend, I., Zhang, C., 2021. Simulating the role of tides and sediment characteristics on tidal flat sorting and bedding dynamics. Earth Surf. Proc. Land. 46, 2163–2176.
Zhu, L., Zhang, G., Zhang, H., Gong, W., Li, S., 2024. Estimation of vertical transport timescales of sediment in the Changjiang Estuary and its adjacent regions. J. Hydrol. 637, 131326. https://doi.org/10.1016/j.jhydrol.2024.131326.
Zuo, L., Roelvink, D., Lu, Y., 2019. The mean suspended sediment concentration profile of silty sediments under wave-dominant conditions. Cont. Shelf Res. 186, 111–126. https://doi.org/10.1016/j.csr.2019.07.016.
Zuo, L., Roelvink, D., Lu, Y., Dong, G., 2021. Process-based suspended sediment carrying capacity of silt-sand sediment in wave conditions. Int. J. Sedim. Res. https://doi.org/10.1016/j.ijsrc.2021.09.007.